Journal of Building Technology, 2024, Volume 6, Issue 2
DOI: 10.32629/jbt.v6i2.2742
ISSN Online: 2717-5103
ISSN Print: 2705-1390

Study on the Performance of Prestressed Concrete Beams Reinforced with Steel Fibers (HPRF)

Siles María, Almenar Martín, Isla Facundo, Luccioni Bibiana

Institute of Structures, School of Exact Sciences and Technology, Universidad Nacional de Tucumán.

Abstract: The addition of fibers to concrete improves the shear performance of a structural element. However, there is a greater amount of scientific work on the evaluation of the effects of fibers in reinforced concrete structural elements than in prestressed elements. In this work, the behavior of HPRF beams tested in shear by other researchers is studied numerically in order to evaluate the contribution of fibers. The objective is to contribute to the efficient design of this type of beams. For this purpose, a shear test is modeled and the parameters of the constitutive model are calibrated by comparing the numerical results with the experimental ones. Then, the numerical model is used to reproduce the behavior of an experimentally tested HPRF beam.

Key words: steel fiber reinforced concrete; prestressed concrete; numerical models

1. Introduction

Prestressed concrete is known to have better structural performance when compared to reinforced concrete. The use of prestressed concrete elements is desirable in many constructions, as it allows for adequate strength to be achieved in structures that require significant development in length, such as bridge spans. In many cases, the use of prestressing can prevent the shear failure that commonly occurs with sudden collapse.

According to numerous studies, the addition of fibers in traditional reinforced concrete beams significantly improves their shear behavior. This statement cannot be directly extrapolated to the behavior of prestressed concrete beams, since, although most studies agree on the beneficial effect of the addition of steel fibers, there are also studies that document a counterproductive effect.

This shows the need, not only for further research on the subject, but also for a deeper analysis of the results obtained so far. An alternative for such analysis is the use of numerical simulation tools. Although existing models have some difficulty in adequately simulating the shear response in both reinforced and prestressed concrete elements, it is very valuable to study them in order to evaluate the range of validity in which they are able to reproduce the experimental response of laboratory tests and to propose improvements in the models or in the calibration that will help to extend this range. Once these limitations are known, numerical modeling allows the simulation of different and varied situations that are costly and difficult to study experimentally.

To this end, the work developed has the following partial objectives: 1) to obtain numerically the response at the material level of fiber-reinforced concrete specimens subjected to shear action while supporting a precompression load

using experimental tests from the literature; 2) to obtain numerically the response of prestressed concrete beams reinforced with steel fibers tested by other researchers.

In general terms, the constitutive models for Fiber Reinforced Concrete (FRC) can be classified according to the scale at which they are defined. In macro-models, the composite material is represented as a single material with average properties. The constitutive laws are obtained from a large number of laboratory tests (Isla, 2014). In this work, the numerical simulations were performed by means of the Ansys Workbench program, using the Menetrey-Willam macro-model.

2. Constitutive Model

To reproduce the behavior of the concrete, an elastoplastic model was used, in which the relationship between the stress tensor σ, the strain tensor ε and the plastic strain tensor ε^{pl} is given by:

$$\boldsymbol{\sigma} = \boldsymbol{C}\,(\boldsymbol{\varepsilon} - \boldsymbol{\varepsilon}^{\boldsymbol{pl}}) \tag{1}$$

Where, *C* is the quarter-order elastic constitutive tensor. This tensor, for an elastic, linear, and isotropic material such as concrete considered at the macroscale, is determined by Young's modulus *E* and Poisson's coefficient μ. The increase of the plastic deformations is calculated by the following flow rule:

$$\dot{\boldsymbol{\varepsilon}}^{\boldsymbol{pl}} = \dot{\lambda}\,\frac{\partial Q_{MW}}{\partial \boldsymbol{\sigma}} \tag{2}$$

Where Q_{MW} is a potential function to be defined later and λ is the plastic multiplier, and the plastic multiplier can be determined by the charge and discharge conditions defined below:

$$f_{MW} \leq 0, \quad \dot{\lambda} \geq 0, \quad f_{MW}\,\dot{\lambda} = 0 \tag{3}$$

Where f_{MW} is the yield surface. This model uses the Menetrey-Willam (1995) yield surface, which is schematized in Fig. 1. Within this surface, the material has an elastic, linear and isotropic behavior. Upon reaching it, the material begins to undergo plastic deformations.

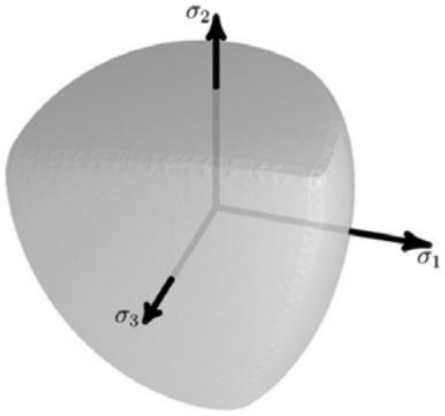

Figure 1. Menetrey-Willam yield surface.

The yield surface is defined as:

$$f_{MW} = \frac{c_2}{c_3}\left[\sqrt{\frac{2}{3}}I_1 + r\sqrt{2J_2}\right] + 2J_2 - \frac{1}{c_3} \tag{4}$$

Where, I_1 is the first invariant of σ and J_2 is the second invariant of the stress deviatoric tensor *S*. In equation (4), c_2, c_3 and *r* depend on material parameters and the hardening and softening functions:

$$c_2 = \frac{1}{\sqrt{6}}\left[\frac{1}{\overline{R_c}} - \frac{1}{\overline{R_b}} + \frac{\overline{R_b} - \overline{R_t}}{\overline{R_c}^2}\right] \quad (5)$$

$$c_3 = \frac{3}{2}\frac{1}{\overline{R_c}^2} \quad (6)$$

$$r = \frac{4(1-e^2)cos^2\theta + (2e-1)^2}{2(1-e^2)\cos\theta + (2e-1)\sqrt{4(1-e^2)cos^2\theta + 5e^2 - 4e}} \quad (7)$$

With:

$$\overline{R_t} = R_t\Omega_{tc}\ ,\ \overline{R_c} = R_c\Omega_c\ ,\ \overline{R_b} = R_b\Omega_c \quad (8)$$

$$\Omega_{tc} = \begin{cases} \Omega_t & \kappa_c \le \kappa_{cm} \\ \Omega_t\Omega_c & \kappa_c > \kappa_{cm} \end{cases} \quad (9)$$

$$\epsilon = \frac{\overline{R_t}}{\overline{R_b}} * \frac{\overline{R_b}^2 - \overline{R_c}^2}{\overline{R_c}^2 - \overline{R_t}^2}\ ,\quad e = \frac{1+\epsilon}{2-\epsilon}, \quad (10)$$

$$\cos 3\theta = \frac{3\sqrt{3}}{2}\frac{J_3}{\sqrt{J_2}^3} \quad (11)$$

Where: R_t, R_c and R_b are the tensile, compressive and biaxial strengths respectively. *Qt* and *Qc* are the hardening and softening functions, respectively depending on Ω_t and Ω_c, which are the tensile and compressive hardening variables respectively. J_ε is the third invariant of the stress stiffener *S*.

$$\dot{\kappa}_c = \frac{\alpha_c}{\overline{R_t}}\boldsymbol{\sigma}\ .\ \dot{\boldsymbol{\varepsilon}}^{\boldsymbol{pl}} \quad (12)$$

$$\dot{\kappa}_t = \frac{\alpha_t}{\overline{R_t}}\boldsymbol{\sigma}\ .\ \dot{\boldsymbol{\varepsilon}}^{\boldsymbol{pl}} \quad (13)$$

Where, $\delta\cdot\boldsymbol{\varepsilon}^{pl}$ represents the increment of plastic work. α_c and α_t are the compressive and tensile weight functions respectively defined as:

$$\alpha_c = 1 - \alpha_t \quad (14)$$

$$\alpha_t = \begin{cases} 0 & \tan\alpha < -2 \\ \frac{1}{1+e^{-10\tan\alpha}} & -2 \le \tan\alpha \le 2 \\ 1 & \tan\alpha > -2 \end{cases} \quad (15)$$

$$\tan\alpha = \frac{I_1}{\sqrt{J_2}} \quad (16)$$

The compression hardening and softening function is defined as:

$$\Omega_c = \Omega_{ci} + (1-\Omega_{ci})\sqrt{2\frac{\kappa_c}{\kappa_{cm}} - \frac{\kappa_c^2}{\kappa_{cm}^2}} \quad \text{for } k_c < k_{cm} \quad (17)$$

$$\Omega_c = 1 - (1-\Omega_{cu})\left(\frac{K-K_{cm}}{K_{cu}-K_{cm}}\right)^2 \quad \text{for } k_{cm} < k_c < k_{cu} \quad (18)$$

$$\Omega_c = \Omega_{cr} + (\Omega_{cu} - \Omega_{cu})e^{\left(2\frac{\Omega_{cu}-1}{K_{cu}-K_{cm}} * \frac{\kappa_c - K_{cu}}{\Omega_{cu}-\Omega_{cr}}\right)} \quad \text{for } k_c > k_{cu} \quad (19)$$

Where K_{cm} and K_{cu} are material parameters corresponding to the value of the compression hardening variable at the transition of its different branches. In particular, K_{cm} is the value of the compression hardening variable at the peak of the Ω_c function and occurs when $\Omega_c = 1$. Ω_{ci} is the initial value of Ω_c, Ω_{cu} is the value corresponding to k_{cu} and Ω_{cr} is the value when K_c tends to infinity.

The hardening and softening function entraction is defined as:

$$\Omega_t = e^{-\frac{\kappa_C}{a_t}} \tag{20}$$

$$a_t = \frac{g_{ft}}{R_t} \tag{21}$$

$$g_{ft} = max(\frac{G_{ft}}{L_i}, \frac{{R_t}^2}{E}) \tag{22}$$

Where g_{ft} is the tensile fracture energy. L_i is the effective length of the element and must be determined so that the following equation is satisfied:

$$\int_0^\infty \Omega_t \, d\kappa_t = \frac{g_{ft}}{R_t}. \tag{23}$$

Fig. 2 shows the typical shape of the hardening and softening functions in tension and compression of concrete. These functions can be obtained from laboratory tests in tensile and uniaxial compression.

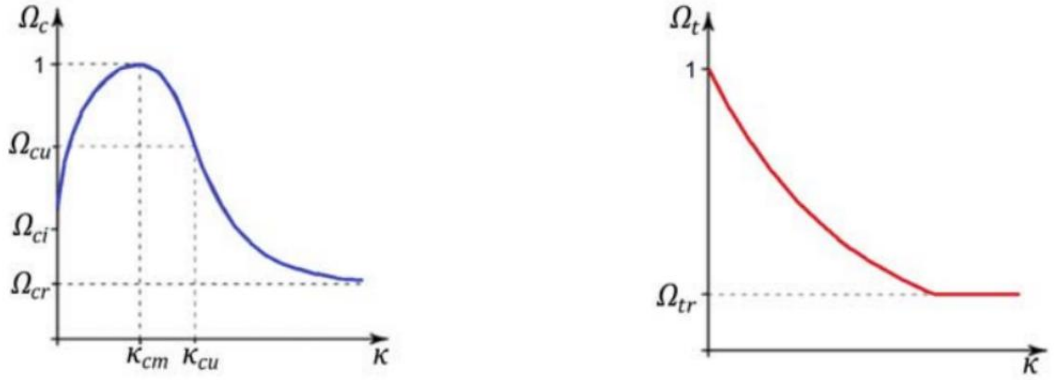

(a) (b)

Figure 2. Hardening and softening functions in (a) compression and (b) tension.

The model uses non-associated flow. The potential function is defined as:

$$Q_{MW} = 2J_2 + B_g\sqrt{2J_2} + C_g\frac{1}{\sqrt{3}}I_1 \tag{24}$$

$$B_g = \frac{2\overline{R_c}\tan\Psi - \sqrt{2}\overline{R_t}}{\sqrt{3}(1-\sqrt{2}\tan\Psi)} \tag{25}$$

$$C_g = \frac{B_g}{\sqrt{2}} + \frac{2\overline{R_t}}{\sqrt{3}} \tag{26}$$

Where Ψ is the angle of dilatancy.

In summary, it can be said that the model has 3 sets of parameters to be defined:

- Elastic Parameters: E and μ.
- Fluence Surface Parameters and Potential Function: R_t, R_c, R_b and Ψ.
- Hardening and softening function parameters: K_{cm}, K_{cu}, Ω_{ci}, Ω_{cu}, Ω_{cr}, Ω_{tr} and G_{ft}.

3. Reproduction of the Modified JSCE Decortication Assay

The research work carried out by Diaz Fontdevila et al. (2021) shows that the model proposed by Menetrey-Willam is able to satisfactorily represent the behavior of the HPRF in shear. However, in this work, it was intended to simulate the response of the HPRF to shear stresses, so the model was evaluated, including the prestressing effect to demonstrate that it is also able to reproduce it adequately.

For this purpose, the modified JSCE (Japan Society of Civil Engineers) direct shear test was modeled, and the numerical results were compared with the experimental values reported by other researchers. In this test, the stress field is very close to the pure shear stress field, making it easier to relate the results to the material's response to shear.

Soetens (2015) used H50 concrete in this experiment, which has high-strength steel fibers and hooks at the ends (yield stress > 2000 N/mm²). He used fibers of two different lengths (60 mm and 30 mm) in combination with a self-compacting concrete and a traditional concrete. The fiber contents used were 20, 40 and 60 kg/m^3.

A schematic of the test setup is shown in Fig. 3.

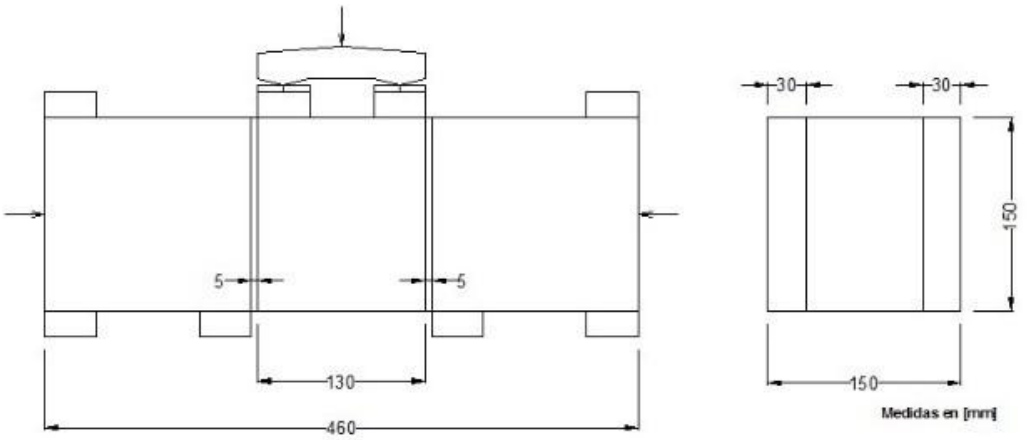

Figure 3. Geometry and support conditions of the modified JSCE test.

In order to obtain predefined crack planes, 30 mm deep cutouts were cut vertically on both sides of the standard prism. Therefore, the dimensions of the cutting plane are 90 × 150 mm². To investigate the effect of confining pressure, further modifications were made to the test setup. A constant horizontal compressive load was applied using a horizontal jack.

The 3D model used to simulate this test is shown in Fig. 4. The face of the support that is in contact with the specimen has a frictional contact, whose friction coefficient is equal to 0.3, called support (A). While the opposite face was considered as a fixed support, called support (B). In addition, the contact between the right base of the loading device and the corresponding support was modeled as frictionless, denoted as support (C). The supports (A), (B) and (C) are shown in Fig. 4. As for the loads, in order to compress the specimen, a longitudinal pressure was applied on the cross section of the specimen, and vertical displacements were applied at the upper edges of the loading device.

The finite element mesh used is shown in Fig. 4. Solid elements of quadratic order defined by 20-node hexahedra and 10-node tetrahedra were used, where each node has 3 degrees of freedom of displacements. It can be seen that in the proximity of the fault plane the mesh refinement increases.

At the points located halfway up the left notch, the displacements in the vertical axis were measured in order to calculate the difference between both values (relative vertical displacement between these points), and then averaged with the value obtained on the back face of the notch. The same was done on the right notch and the values were averaged. These points are indicated in Fig. 4.

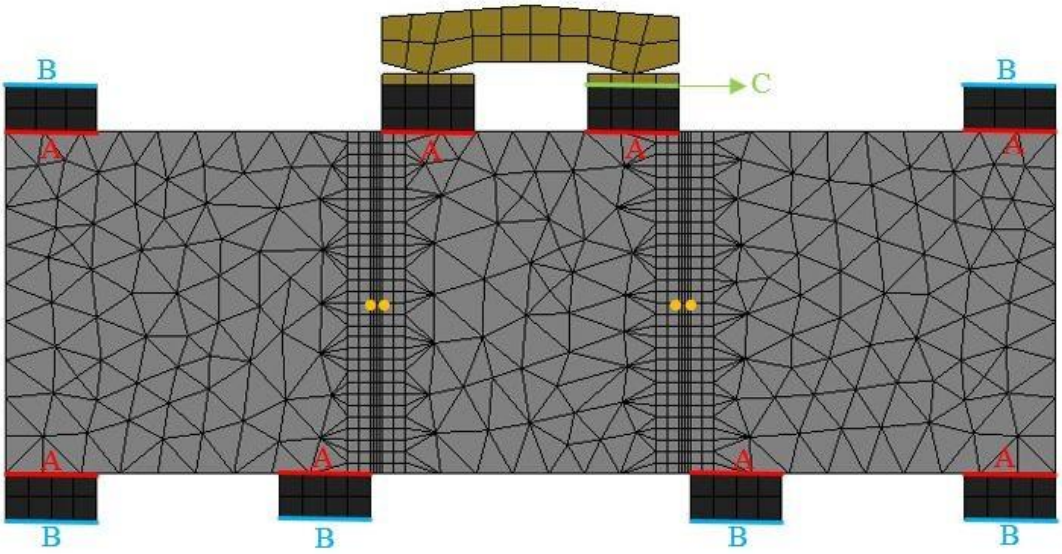

Figure 4. 3D model used. (A) frictional support (B) fixed support (C) frictionless support.
(.) points at which displacement is measured.

The experimental response (without horizontal compression load) of the self-compacting concrete without fibers and with 40 kg/m^3 of 60 mm long steel fibers was adjusted. The calibrated parameters are shown in Table 1.

Table 1. HS and HRF40 model parameters

Parameter	HS	40 kg/m^3
E (MPa)	35000	35000
M	0.2	0.2
R_c (MPa)	50	50
R_t (MPa)	4.8	5.5
R_b (MPa)	58	58
Ψ (°)	10	10
K_{cm}	0.01	0.01
K_{cu}	0.02	0.03
Ω_{ci}	0.33	0.33
Ω_{cu}	0.7	0.99
Ω_{cr}	0.15	0.20
g_{fi} (N/m)	40	800
Ω_{tr}	0.15	0.20

Fig. 5 shows the obtained short-displacement stress-strain curves.

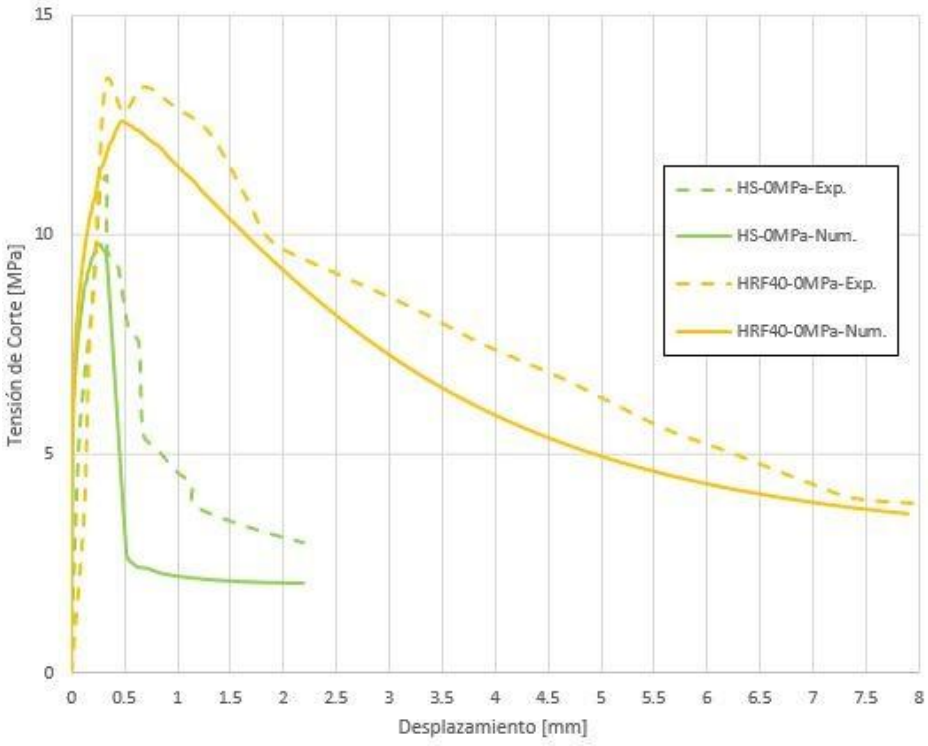

Figure 5. Shear stress-displacement curves HS and HRF40.

Then, a precompression load of 5 and 10 MPa was introduced into the HRF40 model, and shear tests were simulated. Fig. 6 shows the obtained shear-displacement stress curves and their comparison with the experimental results (Soetens, 2015). By increasing the normal stresses, an increase in the shear stresses is obtained over the entire sliding range considered.

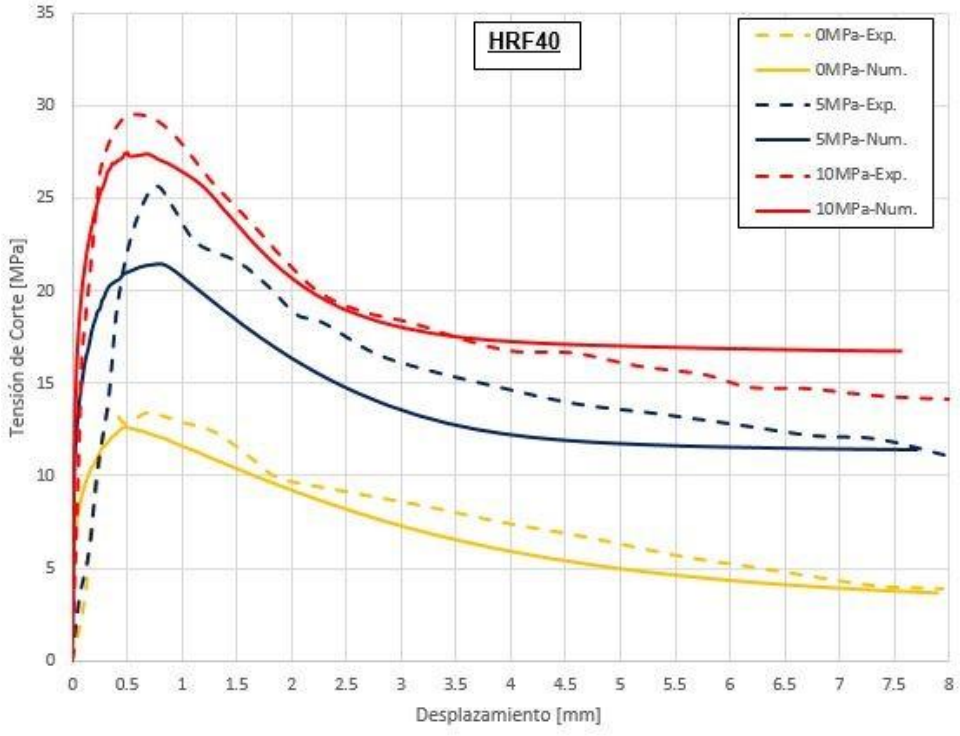

Figure 6. Response to HPRF40 shear.

Fig. 7 shows the equivalent plastic deformation map of one of the specimens. Generalized failure of the notch plane occurs once compressive stresses (in the longitudinal direction) above the limit are reached in the upper part of the notch.

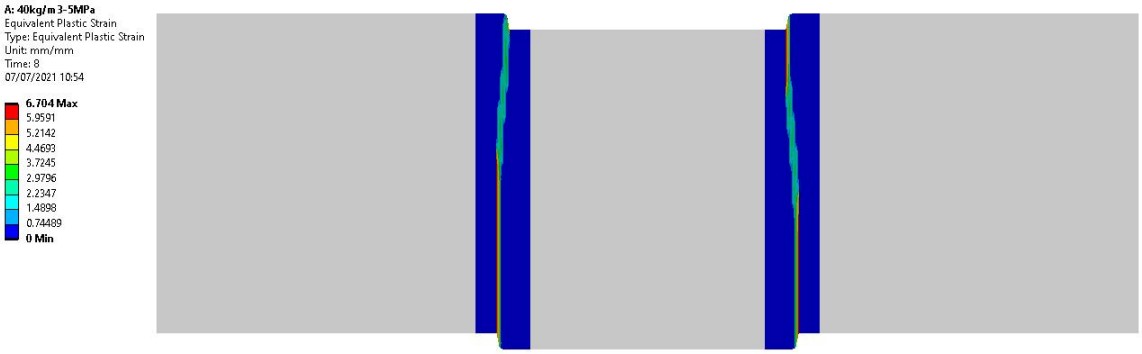

Figure 7. Plastic-equivalent deformation map. HRF40-5MPa. Deformation x1.

4. Application of the Model for HPRF Beams

In this section, it was verified whether the numerical model is able to reproduce the response of prestressed concrete (PC) and HPRF beams made by other researchers, whose configuration leads to shear failure. For this purpose, the experimental tests of Cho et al. (2009) were used.

The geometry of the tested beams is illustrated in Fig. 8 (Cho et al., 2009). A total of 6 prestressing strands of φ = 12.7 mm (ASTMA416, tensile strength of 1860 MPa, normal relaxation) were used in each beam. An initial prestressing of 1303 MPa was applied to each strand. After stress losses, both due to concrete and steel, the effective prestressing value was 1,034 MPa, so the sum of all losses was approximately 20%. Additional non-prestressed steel (7 φ = 25.4 mm distributed in two layers in the bottom fiber, and 2 φ = 12.7 mm in the top fiber), with yield stress of 420 MPa, was used to prevent premature flexural failure.

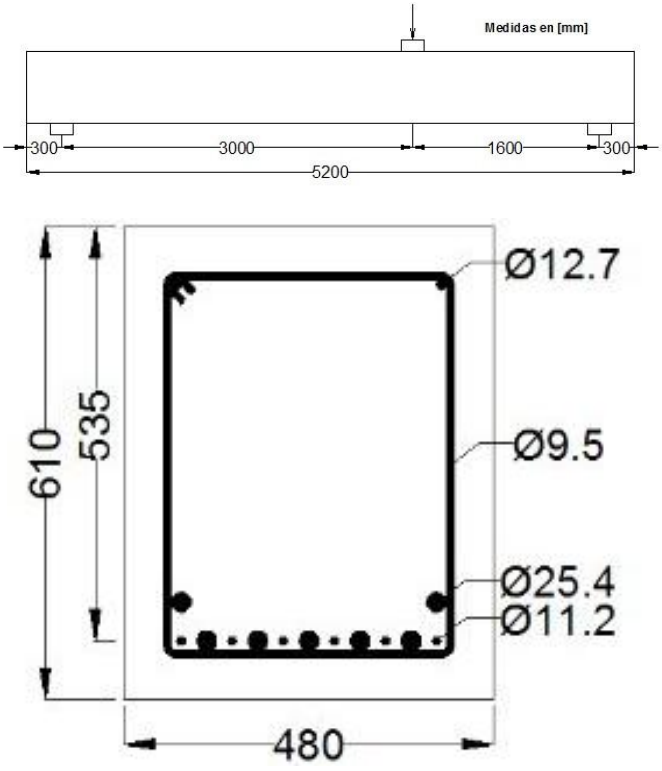

Figure 8. Geometry and support conditions of the test.

The longest span was reinforced with stirrups of φ = 9.5 mm every 200 mm (Fig. 9) to ensure that shear failure occurred in the shear span under investigation. The ratio of the shear span length to the serviceable height is equal to 3.

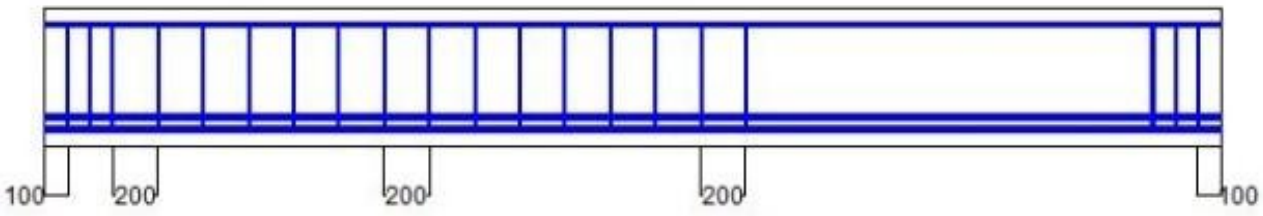

Figure 9. Arrangement of reinforcement.

In addition, the steel fibers used had hooked ends, an aspect ratio of 80 (l_f = 61 mm, d_f = 0.76 mm), and a tensile strength of 1048 MPa. 60 kg/m^3 of fibers were incorporated. This program does not provide the possibility of modeling only prestressed anchor cables, adding concrete, and then releasing the anchor cables, but it was modeled together from the beginning. Then, in order to simulate the effect of prestress, negative temperature changes were introduced in the strands. This makes them tend to shorten themselves, but concrete prevents them. Finally, in order to achieve balance, the rope was tightened and the concrete was compressed, successfully simulating the behavior of prestressing.

The experimental work showed indications of reinforcement slippage, and to explain this effect, the elastic modulus of the steel was reduced by 25%, i.e., E = 150 GPa was used. For the specified compressive strength of the concrete, $f'c$, 80% of the value reported by the researchers (63 MPa) was used, since it was obtained by testing prismatic specimens. On the other hand, in order to avoid the concentration of stresses on the external faces of the beam, a concrete block with linear elastic behavior was added at both ends.

Finally, it should be noted that, although each of the prestressing strands is φ = 12.7 mm, bars with an equivalent diameter of 11.2 mm were modeled in the program, providing the value of the nominal area corresponding to that strand (98.71 mm^2).

Linear finite elements were used. For the concrete, 8-node hexahedral solid elements were used, while 2-node bar elements were used for the reinforcement. The linkage between the concrete elements and the steel elements is specified by the coincidence of nodes between the two elements, so that there is compatibility in the displacements. Figs. 10 and 11 show the finite element meshes adopted.

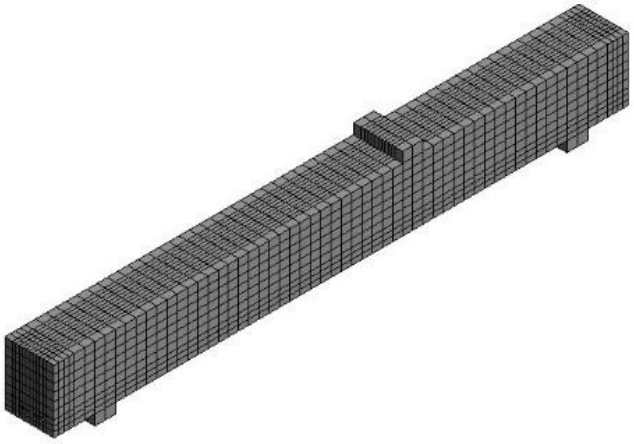

Figure 10. Finite element mesh for concrete.

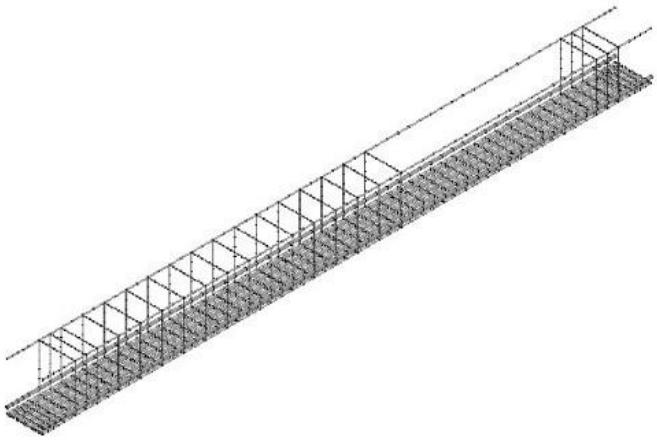

Figure 11. Finite element mesh for steel bars.

Table 2 shows the calibrated parameters for the HP and for the HPRF.

Table 2. Parameters of the HP and HPRF model

Parameter	HP	HPRF
E (MPa)	35,000	35,000
μ	0.2	0.2
Rc (MPa)	50	50
Rt (MPa)	2	3
Rb (MPa)	58	58
Ψ (°)	6	6
K_{cm}	0.0005	0.0005
K_{cu}	0.005	0.05
Ωci	0.4	0.4
Ωcu	0.65	0.65
Ωcr	0.05	0.5
g_{ft} *(N/m)*	20	1200
Ωtr	0.05	0.5

The vertical displacement was measured at the bottom face of the beam section where the load is applied. The load-displacement curves obtained are shown in Fig. 12.

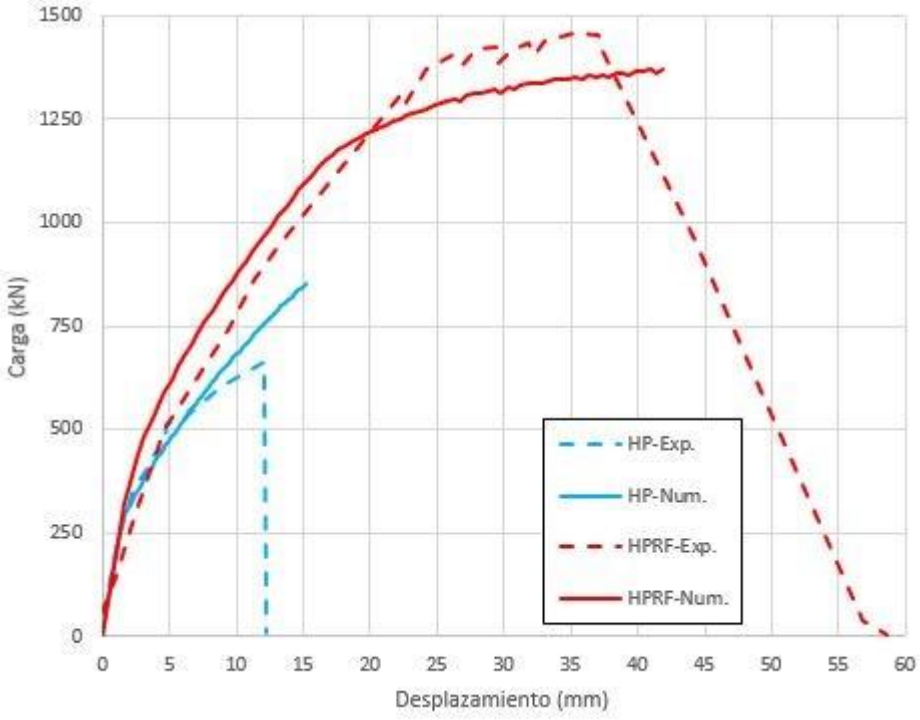

Figure 12. Load-displacement curves of the HP and HPRF.

The numerical results can be considered to satisfactorily reproduce the experimental results. Figs. 13 and 14 show the equivalent plastic deformation maps that qualitatively show the location of the cracks.

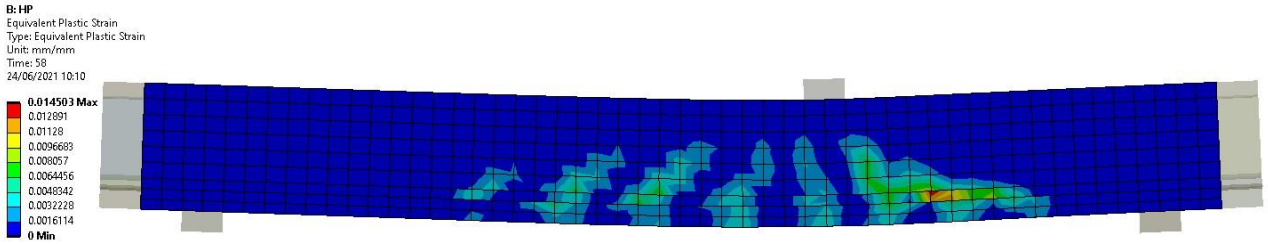

Figure 13. Plastic-equivalent deformation map of the HP. Deformation x5.

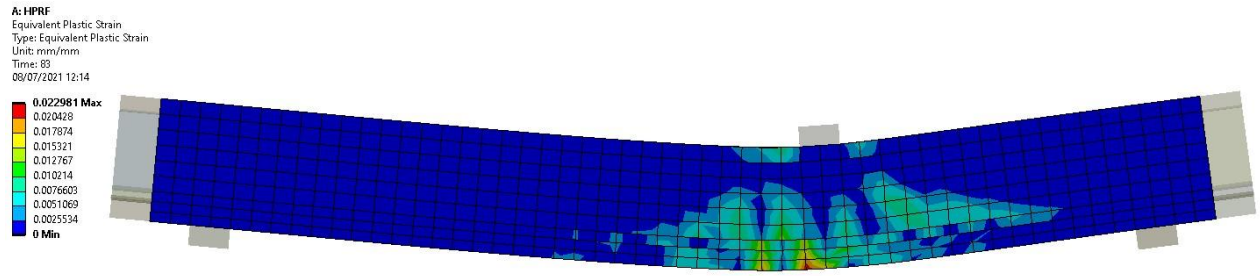

Figure 14. Plastic-equivalent deformation map of the HPRF. Deformation x5.

The characteristic shear failure can be seen in Fig. 13. When fibers are added (Fig. 14), a more distributed cracking pattern is generated, due to the stitching action of the fibers, and the failure mechanism is closer to bending.

5. Conclusions

According to the results obtained with the numerical simulation of the modified JSCE shear test, it can be stated that:

- The numerical model is able to satisfactorily reproduce the behavior at material level during shear failure.

- Experimental values show an increase in the peak load value with the incorporation of fibers. This increase is modeled with a higher tensile strength.

- The relationship between the shear strength and the post-peak points of the hardening and softening function in compression of concrete (k_{cu}, Ω_{cu} and Ω_{cr}) is observed, since these values are higher for HRF40.

According to the results obtained with the numerical simulation of the behavior of HP and HPRF beams under shear failure, it can be said that:

- The effect of the addition of fibers on the strength and ductility of concrete under shear stresses is observed. The shear strength of the HPRF beam was significantly improved by the addition of steel fibers, and higher ductility was obtained compared to the HP beam.

- When fibers are added, the equivalent plastic deformation maps show a more distributed deformation pattern, due to the stitching action of the fibers.

- With the addition of fibers, the stresses in the longitudinal members increase. Therefore, the fibers allow the failure mechanism of the beam to move away from a shear failure mechanism to a flexural failure mechanism.

Acknowledgments

The authors would like to thank the UNT (PIUNT E/623) and CONICET for their support.

Conflicts of Interest

The author declares no conflicts of interest regarding the publication of this paper.

References

[1] Cho J-S., Lundy J., Chao S-H. 2009. Shear strength of steel fiber reinforced prestressed concrete beams, pp. 1058-1066.

[2] Diaz Fontdevila M., Almenar M. 2021. Diseño a cortede elementos de hormigón armado con fibras deacero, Proyecto Final de Carrera de Ingeniería Civil-FACET-UNT.

[3] Dmitriev A., Novozhilov Y., Mikhalyuk D., Lalin V. 2020. Calibration and validation of the menetrey-willam constitutive model for concrete. *Construction of Unique Buildings and Structures*, pp. 88.

[4] Isla Calderón F. 2014. Modelo para hormigones reforzadoscon fibras de acero, Tesis Doctoral-FACET-UNT.

[5] Soetens T. 2015. Design models for the shear strength of prestressed precast steel fibre reinforced concrete girders, Faculty of Engineering and Architecture Ghent University-Belgium.